VIRTUAL AND PHYSICAL PROTOTYPING
2026, VOL. 21, NO. 1, e2637380 (19 pages)
https://doi.org/10.1080/17452759.2026.2637380

Taylor & Francis
Taylor & Francis Group

Multi-material 3D printed compression-induced stretching lattice metamaterials with superior reusable energy absorption

Haitao Ye[a]*, Xingjian Huang[b]*, Liuchao Jin[a], Sicong Zhou[a], Guoquan Xie[a], Zongxin Hu[a], Rui Li[a], Haoming Mo[a], Shitong Fang[c], Wei-Hsin Liao[a], Qi Ge[b] and Xu Song[a]

[a]Department of Mechanical and Automation Engineering, The Chinese University of Hong Kong, Shatin, Hong Kong SAR; [b]Shenzhen Key Laboratory for Additive Manufacturing of High-Performance Materials, Department of Mechanical and Energy Engineering, Southern University of Science and Technology, Shenzhen, People's Republic of China; [c]Guangdong Key Laboratory of Electromagnetic Control and Intelligent Robots, College of Mechatronics and Control Engineering, Shenzhen University, Shenzhen, People's Republic of China

ABSTRACT

Achieving high-efficiency energy absorption while maintaining structural recoverability remains a critical challenge in lattice structure design, as conventional materials often sacrifice load-bearing capacity for reusability. To address this trade-off, we propose a reusable compression-induced stretching (CIS) lattice metamaterial fabricated via multi-material 3D printing. Our design employs a 'wrapping' strategy to ensure robust integration between the rigid skeleton and the soft dissipative phase. Unlike conventional lattices that rely on unstable buckling, our metamaterial utilises rationally designed geometric nonlinearity to convert global compression into uniform stretching of embedded viscoelastic sheets. Consequently, it exhibits an energy absorption capacity that is 358.5% higher than that of bending-dominated designs and sustains stable hysteresis loops over 500 cycles with negligible residual strain. Furthermore, the mechanical response is highly programmable: by tailoring intra-cell size, material gradients, and global aspect ratios, the deformation sequence can be designed to achieve progressive densification. Finally, we demonstrate the scalability of this concept by constructing a macroscopic 3D cylindrical metamaterial, thereby providing a versatile platform for next-generation reusable energy-absorbing systems.

ARTICLE HISTORY
Received 5 February 2026
Accepted 20 February 2026

KEYWORDS
Mechanical metamaterial; compression-induced stretching mechanism; energy absorption; reusability; multi-material 3D printing

1. Introduction

Energy-absorbing structures [1,2] are ubiquitous in engineering, playing important roles in impact mitigation for personal protective equipment, automotive crashworthiness, and the packaging of delicate instruments. These systems are fundamentally characterised by their hysteretic force-displacement responses [3], which are typically engineered to maintain a manageable peak force while maximising stroke length to optimise energy absorption. Conventionally, energy absorbers – such as foams [4,5], ceramics [6,7], and metals [8–10] – rely predominantly on irreversible mechanisms, including plastic deformation, fragmentation, and molecular bond breakage. While effective, their 'single-use' nature necessitates costly replacements and contributes to material waste, rendering them unsuitable for applications requiring repetitive impact protection [11,12].

To overcome the inherent limitations of disposable systems, a paradigm shift has emerged toward developing reusable energy-absorbing metamaterials via damage-tolerant micro-lattice designs [13–15], multistable structure designs [16–19], and others. Unlike bulk materials, these mechanical metamaterials [20–27] derive their unique properties from a rationally designed mesostructure rather than chemical composition alone. A prevailing strategy involves exploiting elastic instabilities – such as the snapping of bistable curved beams [28] or the buckling of tilted struts [18] – where energy is dissipated through reversible elastic deformation. However, a critical trade-off remains: purely elastic metamaterials often suffer from low energy absorption efficiency (characterised by narrow hysteresis loops) compared to their plastic counterparts. Furthermore, designs prioritised for high resilience frequently sacrifice load-bearing capacity, creating a technological

CONTACT Qi Ge geq@sustech.edu.cn Shenzhen Key Laboratory for Additive Manufacturing of High-Performance Materials, Department of Mechanical and Energy Engineering, Southern University of Science and Technology, Shenzhen 518000, People's Republic of China; Xu Song xsong@mae.cuhk.edu.hk Department of Mechanical and Automation Engineering, The Chinese University of Hong Kong, Shatin, Hong Kong SAR
*These authors contributed equally to this work.

gap between robust reusability and high-performance energy absorption.

While current reusable metamaterials capitalise primarily on simple mechanical buckling [11,29] or inter-component friction [12,30], we propose an alternative design – the compression-induced stretching (CIS) system – to construct high load-bearing energy absorbers with reusability. Conceptually, the design features a unit cell comprising rigid blocks connected diagonally via flexible hinges, bridged by viscoelastic tensioning sheets. Unlike conventional lattices where collapse is governed by bending [31,32], our lattice harnesses geometric nonlinearity: upon reaching a critical threshold, the compressive load triggers a coordinated rotation of the rigid blocks, which mechanically drives the deformation mode of the soft sheets from potential buckling to significant stretching. By integrating viscoelastic elastomers as the tensioning elements, this mechanism effectively activates the material's internal viscous damping over a large volume, generating a substantial hysteresis loop while ensuring autonomous recovery upon unloading.

However, physically realising such heterogeneous architectures – where rigid kinematics must seamlessly couple with soft dissipative elements – remains a formidable challenge for conventional manufacturing [33] (e.g. moulding or laser cutting). To bridge this gap, multi-material additive manufacturing (AM) technologies [34], including Direct Ink Writing (DIW), Digital Light Processing (DLP), and Fused Deposition Modelling (FDM), have been extensively explored. Among these, multi-material FDM technology is particularly favoured for its scalable print area, cost-effectiveness, and material versatility. Nevertheless, the mechanical performance of multi-material FDM 3D printed parts is critically contingent upon the interfacial bonding strength between dissimilar materials. To ensure structural integrity, researchers have developed interface reinforcement strategies such as macroscopic overlapping and mechanical interlocking [35,36]. Notably, the 'wrapping' technique, which utilises a tough soft matrix to physically encapsulate rigid reinforcements, has proven highly effective in achieving robust interfaces within multi-material FDM printed structures [37,38].

Here, we present a systematic investigation into the reusable, high-load-bearing CIS metamaterial. We emphasise that the desired kinematic behaviour is strictly contingent upon specific geometric constraints. Through a combined experimental and numerical approach, we identify a critical bifurcation boundary where improper designs trigger an unfavourable 'inward rotation' (Compression-induced Bending, CIB) rather than the target 'outward rotation' (CIS). By establishing a comprehensive design map to delineate the valid parameter space, we ensure the activation of the efficient tensile mode. Consequently, the proposed metamaterial demonstrates a superior balance of longevity and efficiency, sustaining competitive energy absorption even after 500 loading cycles. Furthermore, we extend this framework by customising the deformation sequence through size effect, gradient design, and geometric aspect ratio, demonstrating the system's high programmability and validating its macroscopic scalability through a 3D cylindrical structure, ultimately providing a versatile solution for next-generation reusable energy absorption systems.

2. Materials and methods

2.1. Design and fabrication of the CIS metamaterial

The physical realisation of the proposed CIS metamaterials necessitates a manufacturing approach capable of seamlessly integrating disparate mechanical phases – specifically, rigid kinematics and soft dissipation – without compromising structural integrity. To address the persistent challenge of weak interfacial bonding in multi-material additive manufacturing, we implemented a robust 'wrapping' strategy utilising a commercial dual-extrusion FDM system (Bambu Lab, China), as illustrated in Figure 1a. Unlike conventional layer-stacking methods prone to delamination, our approach involves embedding the rigid polylactic acid (PLA) 'skeleton' within a continuous thermoplastic polyurethane (TPU) 'matrix'. Crucially, this geometric continuity of the flexible phase ensures that stress is effectively transferred across the hinges and tensile sheets, preventing interfacial failure even under the substantial elongation induced by the CIS mechanism.

Beyond guaranteeing interfacial integrity, this wrapping strategy imparts intrinsic robustness against artifacts inherent to the FDM process. The soft TPU layer acts as a buffer that effectively mitigates stress concentrations at the rough, layer-wise interfaces of the printed PLA core. Crucially, the printing path of the TPU sheets is aligned longitudinally with the stretching direction. This orientation ensures that tensile loads are borne by continuous filament strands rather than weak inter-layer bonds, thereby maximising tear resistance and energy absorption capability. Furthermore, in macroscopic lattices, the interconnectivity between unit cells imposes kinematic constraints that suppress localised rotation modes caused by minor hinge thickness variations, ensuring the global dominance of the

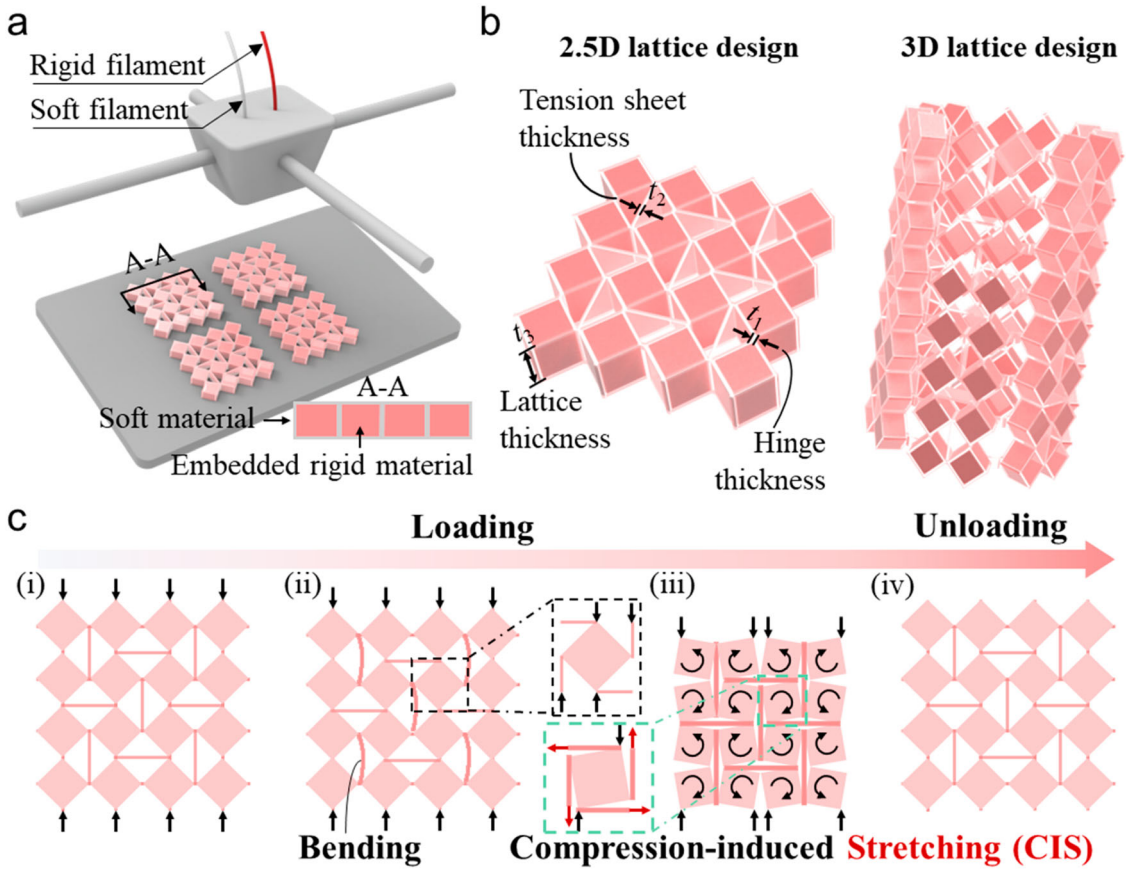

Figure 1. Design and fabrication of the CIS metamaterial. (a) Fabrication of the CIS metamaterial via multi-material FDM 3D printing using the wrapping strategy. **(b)** Geometric designs of the 2.5D and 3D CIS metamaterials. **(c)** Schematic of the deformation process during the loading-unloading cycle: (i) initial compression; (ii) axial compression accompanied by the bending of the stretchable sheets; (iii) outward rotation of the rigid blocks driving the stretchable sheets from a compressed to a stretched state; (iv) recovery of the metamaterial to its initial configuration upon unloading.

energy-efficient stretching mode despite geometric tolerances.

With the fabrication robustness established, the specific geometry of the lattice design, as depicted in Figure 1b, is parametrically defined by three critical geometric variables: the hinge thickness (t_1), the tensile sheet thickness (t_2), and the out-of-plane depth (t_3). These parameters not only dictate the mechanical performance but also govern the bifurcation behaviour of the unit cells typically arrayed in 2.5D or 3D configurations.

The fundamental working principle of the CIS system relies on a geometry-induced mode transition, as demonstrated in Figure 1c. The deformation sequence proceeds in three distinct stages: (i) Initial Loading: Under axial compression, the structure undergoes linear elastic deformation where the load is shared by the rigid blocks and flexible hinges. (ii) Kinematic Bifurcation: Upon surpassing a critical geometric instability threshold, the rigid blocks are triggered to rotate relative to the hinges. In a successfully designed CIS unit, this rotation is directed outwardly, thereby dictating the kinematics of the system. (iii) Viscoelastic Dissipation: This outward rotation converts the global compressive displacement into localised, high-strain uniform stretching of the TPU sheets. This mode transition activates the viscous damping potential of the stretchable sheets over a large volume, maximising energy dissipation. Finally, upon unloading, the stored elastic strain energy within the stretched sheets acts as a restoring force to drive the self-recovery of the metamaterial to its original configuration, thereby ensuring robust reusability.

2.2. Quasi-static compressions

Quasi-static compression tests were conducted to evaluate the mechanical performance of both the 2.5D and 3D CIS lattice metamaterial specimens. These experiments were performed using a high-precision MTS universal testing machine equipped with a 10 kN load cell, operating at a speed of 9.5 mm/min. This specific loading rate

was chosen to balance experimental standardisation and quasi-static requirements. For the 2 × 2, 2 × 4 (4 × 4), 2 × 6, 2 × 8 samples, the target displacements are 9.5, 19, 28.5, and 38 mm, respectively. This loading rate ensures that the normalised loading duration of a basic unit (2 × 2) is exactly 1 min, facilitating consistent time analysis of the viscoelastic response while strictly maintaining quasi-static conditions to eliminate inertial effects. Energy absorption (EA) is calculated by integrating the area enclosed by the force-displacement curve, while specific energy absorption (SEA) is defined as the ratio of EA to the mass of the sample.

2.3. Constitutive modelling of TPU material

To accurately capture the complex mechanical behaviour of the TPU material-specifically its large deformation hyperelasticity, strain value-dependent stress softening (Mullins effect), and hysteresis (viscoelasticity) – a comprehensive constitutive framework was established. We employed a hybrid material constitutive model (Figure 2a) combining the Yeoh hyperelastic formulation, the Ogden-Roxburgh damage model, and a nonlinear viscoelastic parallel rheological framework.

2.3.1. Yeoh model

The instantaneous elastic response of the TPU is described using the third-order Yeoh hyperelastic potential [39], which was selected for its proven ability to capture the upturn of the stress – strain curve at large elongations. Following the standard isochoric–volumetric split, the strain energy density function W is expressed as:

$$W = \sum_{i=1}^{3} C_{i0}(\bar{I}_1 - 3)^i + \sum_{i=1}^{3} \frac{1}{D_i}(J_{el} - 1)^{2i}, \tag{1}$$

where J_{el} denotes the elastic volume ratio used in the volumetric penalty term. In the present work, the inelastic and viscous deformation are assumed to be isochoric (i.e. no volumetric inelastic strain), so $J_{el} = J = \det(\mathbf{F})$, where $\mathbf{F}$ is the deformation gradient and J is the total volume ratio. The right Cauchy – Green deformation tensor is defined as $\mathbf{C} = \mathbf{F}^{\mathrm{T}}\mathbf{F}$, and its first invariant is $I_1 = \mathrm{tr}(\mathbf{C})$. The isochoric first invariant is $\bar{I}_1 = J_{el}^{-2/3} I_1$. The material constants C_{i0} govern the deviatoric shear response, while D_i control the compressibility. Based on the experimental fitting, the specific material parameters were determined as $C_{10} = 9.207$ MPa, $C_{20} = -1.213$ MPa, $C_{30} = 0.177$ MPa, and $D_1 = 0.0023$ MPa^{-1}, ensuring an accurate representation of the nonlinear stiffening behaviour.

2.3.2. Mullins effect

To characterise the stress softening phenomenon observed during the initial loading-unloading cycles, the constitutive model incorporates the Mullins effect [40] based on the Ogden-Roxburgh framework. This is achieved by introducing a damage variable, η, which modifies the deviatoric strain energy density ($\tilde{W}_{dev}$) of the primary hyperelastic network:

$$U = \eta \bar{W}_{dev} + \phi(\eta) + U_{vol}. \tag{2}$$

The evolution of the damage variable η is governed by the maximum thermodynamic energy density experienced by the material during its deformation history ($W_{\max}$). The damage evolution function is defined using the error function:

$$\eta = 1 - \frac{1}{r} erf\left(\frac{W_{\max} - \tilde{W}_{dev}}{m + \beta W_{max}}\right), \tag{3}$$

where r, m, and β are dimensionless material parameters controlling the extent and rate of damage accumulation. In this study, the parameters were calibrated as $r = 1.448$, $m = 2.598$, and $\beta = 0.060$, which effectively capture the stabilised stress-strain loops after the initial 'break-in' cycles.

2.3.3. Nonlinear viscoelasticity

To account for the hysteresis, a nonlinear viscoelastic network was superimposed onto the hyperelastic-damage framework. This was implemented using a parallel rheological network where the viscous flow is governed by a strain-hardening power law. The creep strain rate ($\dot{\varepsilon}^{cr}$) is defined as:

$$\dot{\varepsilon}^{cr} = \dot{\varepsilon}_0 \left(\frac{\tilde{q}_{eff}}{q}\right)^n (t_{total})^m, \tag{4}$$

Where $\tilde{q}_{eff}$ is the effective von Mises equivalent stress, and t_{total} represents the total time. The specific viscous parameters identified for the TPU material are the effective stress scalar $q = 2.783$ MPa, the power-law exponent $n = 5.184$, the time-hardening exponent $m = -0.002$, and the reference strain rate $\dot{\varepsilon} = 0.783$ s^{-1}. Furthermore, the stiffness ratio ($S_{ratio} = 0.619$) defines the relative contribution of the viscoelastic network to the total stiffness.

This integrated constitutive model (Yeoh + Mullins + Viscoelasticity) was implemented in the ABAQUS/Explicit solver to accurately capture the material's mechanical response. As evidenced in Figure 2b, the simulation results demonstrate excellent agreement with the experimental cyclic loading-unloading curves of TPU material at both 50% and 100% strain levels, confirming

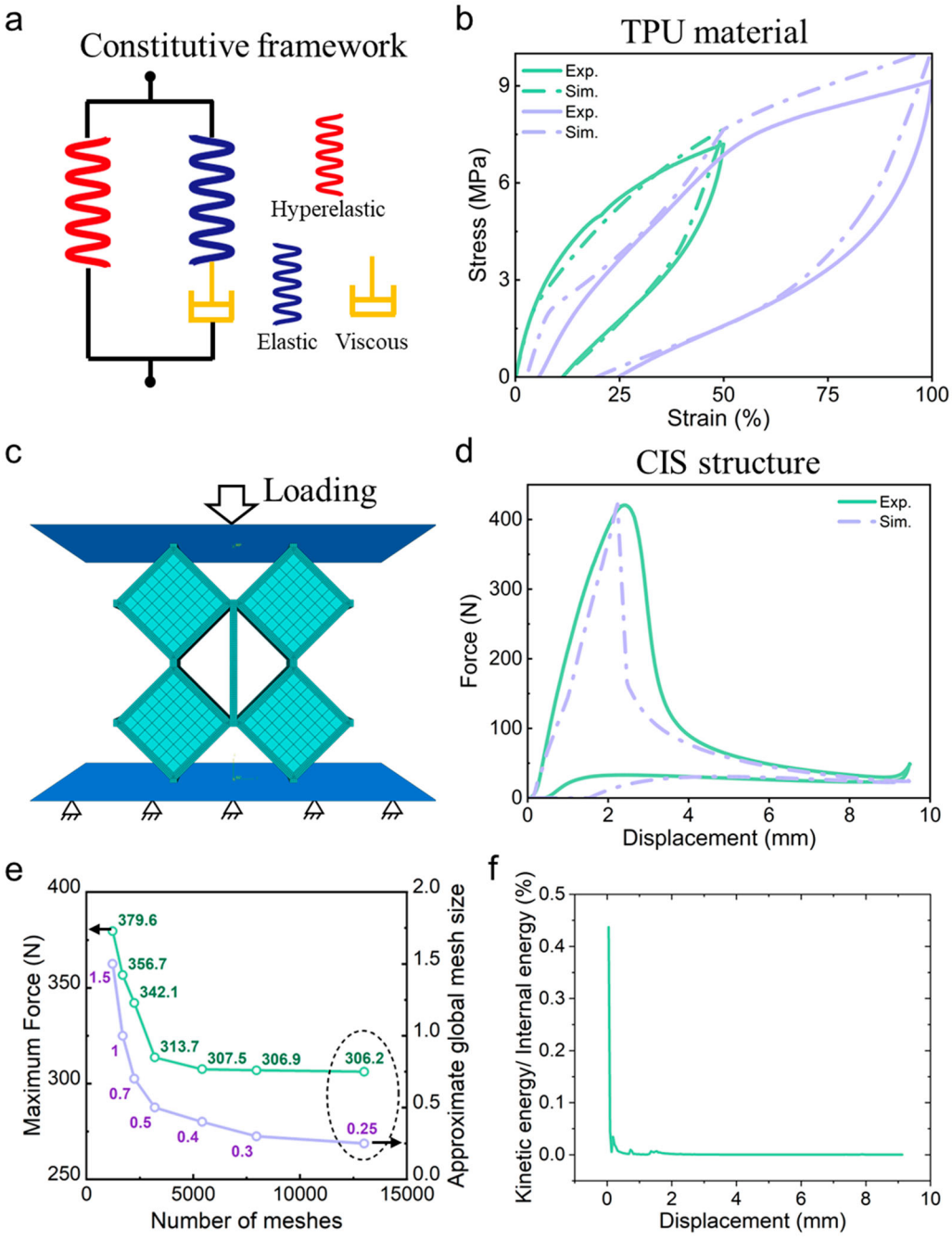

Figure 2. Constitutive modelling and finite element model setup. (a) Constitutive framework characterising the complex mechanical behaviours of the TPU material, including hyperelasticity, the Mullins effect, and viscoelasticity. **(b)** Validation of the material model showing experimental versus simulated cyclic loading-unloading curves at both 50% and 100% strain levels. **(c)** Finite element modelling of the CIS structure. **(d)** Comparison of the experimental and numerical mechanical responses for the CIS structure. (**e**) Mesh convergence analysis. (**f**) Stability Analysis during Compression.

the model's high fidelity in predicting energy absorption and stiffness evolution.

2.4. Finite element model setup

Finite element analysis (FEA) was employed to corroborate the experimental findings and elucidate the underlying mechanical mechanisms of the CIS metamaterials. Geometric modelling was performed using SOLIDWORKS (Dassault Systèmes), while numerical simulations were executed via the ABAQUS/Explicit solver (Dassault Systèmes). Based on a mesh convergence study (Figure 2e), the numerical models were discretized using 8-node linear brick elements (C3D8) with

a global seed size of 0.25 mm. This discretization strategy struck an optimal balance between computational efficiency and solution fidelity. Inter – and intra-structural interactions were managed through the general contact algorithm, characterised by a tangential friction coefficient of 0.07 and a 'hard' contact property for normal behaviour. To replicate quasi-static compression within the explicit dynamic framework, a loading velocity of 2 mm/s was selected, guided by a speed sensitivity analysis (Figure 2f). Throughout the simulation, the ratio of kinetic energy to internal energy remained consistently below 5%, confirming that dynamic inertial effects were negligible.

Building upon this numerical framework, a 2×2 CIS unit model was established in ABAQUS, as illustrated in Figure 2c. The thickness parameters were set to $t_1 = t_2 = 1$ mm, $t_3 = 10$ mm. The rigid materials – PLA were modelled as a linear elastic material with a Young's modulus of 2.75 GPa, a Poisson's ratio of 0.3, and a density of 1.2 g/cm^3. The flexible materials utilised the constitutive model for TPU material as explicitly defined in Section 2.3. Boundary conditions were applied by fully constraining the bottom plate, while a displacement load was applied to the top plate, with all degrees of freedom restricted except for the loading direction. Figure 2d presents the comparative analysis between the experimental and numerical results for the CIS metamaterials. The simulated force-displacement curves exhibit excellent agreement with the experimental data throughout the entire loading-unloading cycle. This high level of fidelity validates the accuracy of the proposed model, confirming its suitability for the subsequent studies of CIS metamaterials.

3. Results and discussions

3.1. Verification of CIS mechanism and cyclic reusability

To investigate the mechanical performance advantages enabled by the CIS mechanism, a series of cyclic compression tests were conducted. Two lattice configurations were evaluated for comparison: a baseline model ('2×2-no sheet') and the proposed CIS model ('2×2-with sheet'), where 'sheet' denotes the stretchable TPU sheets connecting the distal ends of the rigid blocks. As illustrated in Figure 3a, the mechanical response during the first compression cycle revealed a fundamental divergence in deformation modes. The baseline 2×2-no sheet sample exhibited a high initial peak force (523.9 N); however, this was immediately followed by a sharp drop to approximately 33.8 N within a negligible displacement of 0.5 mm, indicating a catastrophic structural instability (or 'snap-through' buckling). In distinct contrast, the 2×2-with sheet sample demonstrated a progressive force softening behaviour, extending the stroke significantly. Upon complete unloading, both samples exhibited negligible residual deformation. Notably, the 'no-sheet' design exhibits a higher initial peak force compared to the CIS lattice, this is because it maintains its structural stability until a higher critical load, whereas the introduction of the soft sheet in the CIS design acts as a lead-in imperfection, triggering the rotational instability earlier and thus lowering the initial peak force.

More significant differences emerged during subsequent cyclic loading (Figure 3b). From the 2nd to the 10th cycle, the reference sample almost completely lost its load-bearing capacity (peak load < 10 N) and energy absorption capacity, effectively behaving like a failed structure. Conversely, the CIS sample maintained robust hysteresis loops with peak reaction forces consistently exceeding 150 N, highlighting its exceptional resilience.

Mechanistically, the selection of the rotation pathway is a symmetry-breaking phenomenon governed by the system's total potential energy landscape. This behaviour is analogous to that observed in bistable compliant structures, where the deformation trajectory is deterministically selected by the specific topography of energy barriers [26]. While the kinematic framework could theoretically allow for either inward or outward rotation, the specific competition of forces – analyzed in Figure 3c – dictates which path deterministically minimises the energy expenditure. In the baseline scenario, the motion of rigid blocks is dictated by the inward component of the hinge tensile force (F_t), friction (f), and the hinge bending moment (M_1). Since friction was minimised via lubrication, the rigid blocks undergo inward rotation (buckling) as soon as the moment induced by F_t overcomes the hinge's bending resistance (M_1), as this represents the path of least resistance for an unconstrained skeleton. Conversely, in the CIS system, the stretchable sheets generate a critical upward force component (F_{s2}), effectively reshaping the energy landscape and lowering the energy barrier for outward rotation. Once the moment generated by F_{s2} exceeds the hinge resistance (M_2), it drives an outward rotation of the rigid blocks. This kinematic guidance ensures that the system follows an energetically favourable pathway that activates the stretch-dominated deformation of the TPU sheets (the CIS mechanism). Even though the hinges experience viscoelastic hysteresis, the presence of these sheets regulates the rotation, delaying instability and maintaining peak reaction forces above 150 N during reloading.

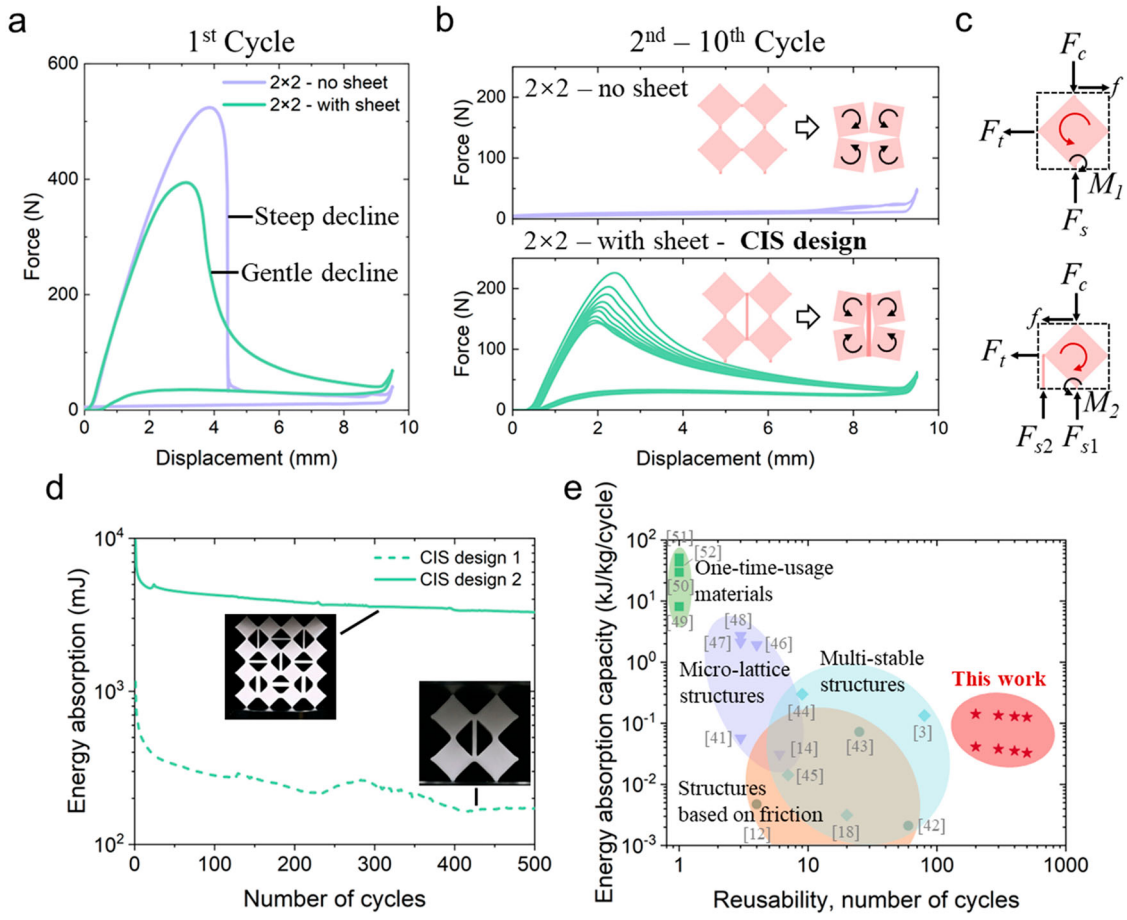

Figure 3. Energy absorption capabilities and reusability of the CIS design. (a) Mechanical response of the baseline 2 × 2 structure and the 2 × 2 – CIS structure during the first compression cycle. **(b)** Cyclic loading-unloading curves of both structures from the 2nd to the 10th cycles. **(c)** Comparative static mechanical analysis of the baseline 2 × 2 and the 2 × 2 – CIS structures. **(d)** Evolution of energy absorption for CIS structures over 500 cycles. **(e)** Comparison of energy-absorbing capacity versus reusability between existing designs in the literature and the proposed CIS metamaterials.

To further evaluate the cyclic durability and long-term energy absorption capabilities essential for practical applications, continuous 500-cycle compression tests were performed on both a single unit cell ('CIS design 1') and a multi-layer array ('CIS design 2'). As shown in Figure 3d, both designs maintained positive energy absorption throughout the entire 500 cycles without exhibiting fracture or delamination, confirming their robust structural integrity. While the energy absorption capacity naturally attenuated during the initial cycles – a phenomenon attributed to the Mullins effect (stress softening) and viscoelastic conditioning of the TPU – it rapidly stabilised. After 500 cycles, CIS design 1 retained 172.03 mJ per cycle (a 77.2% reduction compared to the 2nd cycle), and CIS design 2 retained 3288.9 mJ (a 49.9% reduction).

Furthermore, the performance of the proposed metamaterial was benchmarked against state-of-the-art reusable energy absorbers reported in recent literature [3,12,14,18,41–52]. Figure 3e plots the SEA per cycle against the cycle number. Compared to existing solutions that rely on micro-damage tolerance, multi-stability, or friction-based absorption, the CIS lattice demonstrates a superior balance of longevity and efficiency. Remarkably, it sustains a competitive SEA of 0.126 kJ/kg per cycle even after 500 loading cycles, during which structural integrity was fully maintained without visible delamination. This exceptional durability is underpinned by the 'wrapping' design; although the modulus mismatch between phases presents a theoretical risk of fatigue, this strategy effectively transfers large deformations to the compliant TPU phase while the PLA core remains largely within its elastic regime. The resulting stable mechanical response suggests that the interface bonding is sufficiently tough to arrest micro-crack propagation, thereby validating the robustness of the CIS mechanism for long-term, reusable applications.

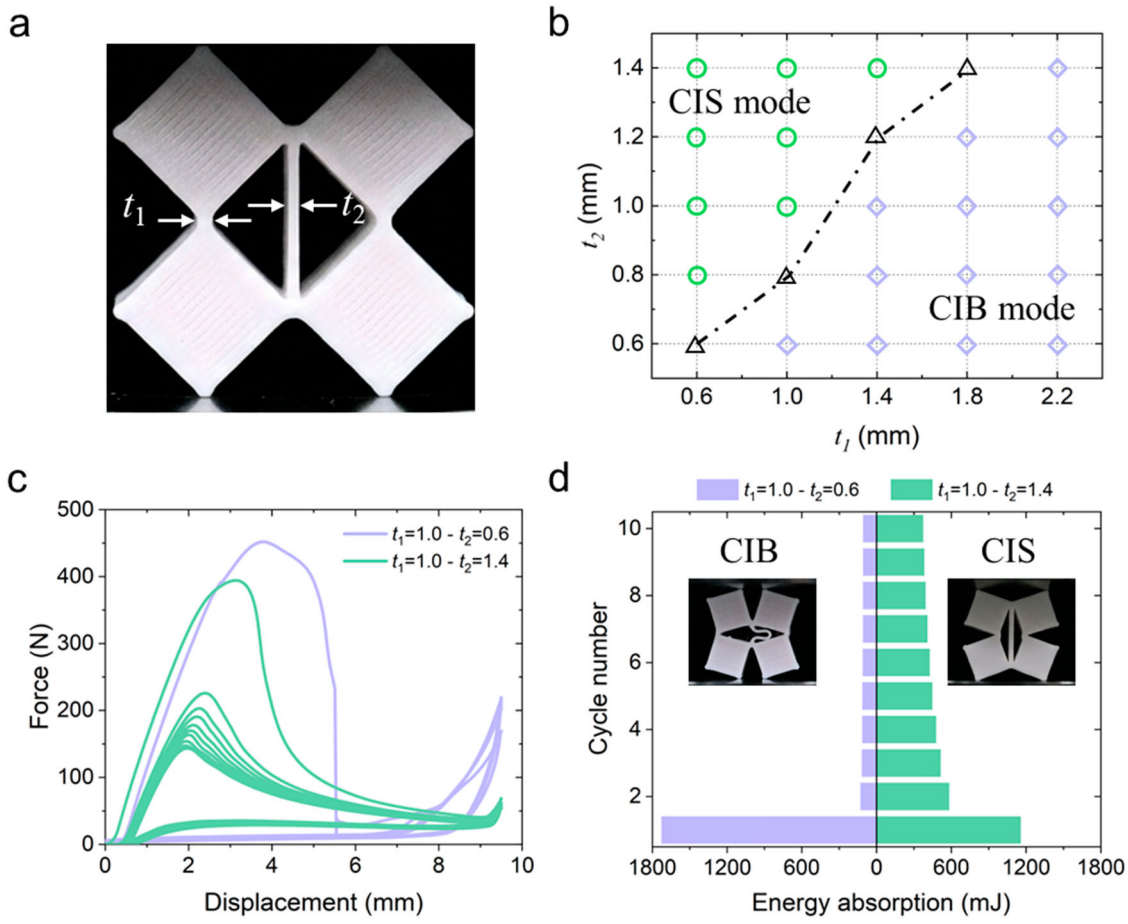

Figure 4. Parametric study and deformation mode analysis. (**a**) Photographs of the fabricated structure and definition of geometric parameters. (**b**) Diagram of deformation modes with respect to structural parameters, where the hinge length *l* was maintained at a constant value of 1 mm. (**c**) Cyclic loading-unloading results for the structure exhibiting the CIB mode (Design 3: $t_1 = 1.0$ mm, $t_2 = 0.6$ mm) and the CIS mode (Design 4: $t_1 = 1.0$ mm, $t_2 = 1.4$ mm). (**d**) Comparison of energy absorption performance between the CIS and CIB modes over 10 cycles.

3.2. Deformation mode transition via geometry design

We emphasise that the advantageous CIS mode is not intrinsic to the material but solely depends on the geometric design, which governs the bifurcation behaviour by shaping the unit cell's potential energy landscape. To clarify this governing role, a systematic parametric study was conducted involving the hinge thickness (t_1) and the TPU sheet thickness (t_2), as illustrated in Figure 4a. Figure 4b presents the resulting deformation modes diagram. A clear kinematic bifurcation is observed: (1) CIB Domain (Purple diamonds): Configurations with $t_1 > t_2$ primarily exhibit the CIB mode, where inward rotation causes inefficient sheet buckling. (2) CIS Domain (Green circles): Configurations with $t_1 \leq t_2$ facilitate the desired CIS mode. This boundary correlates well with the static analysis in Figure 3c: a thicker hinge (larger t_1) imposes a higher bending resistance moment (M_2), elevating the energy required for outward rotation. Consequently, a sufficiently thicker TPU sheet (larger t_2) is required to generate a counteracting moment to overcome M_2. From an energy perspective, the condition $t_1 \leq t_2$ ensures that the 'outward' mode minimises the initial bending energy required at the hinges while most efficiently transitioning the external work into the stretching of the soft phase, thereby ensuring the global dominance of the energy-efficient CIS mechanism.

To quantify the impact of this mode transition, two representative designs – Design 3 ($t_1 = 1.0$, $t_2 = 0.6$, CIB mode) and Design 4 ($t_1 = 1.0$, $t_2 = 1.4$, CIS mode) – were subjected to cyclic loading (Figure 4c). Although Design 3 showed a higher initial peak force, it suffered from immediate instability and negligible performance in subsequent cycles. In contrast, Design 4 maintained robust mechanical performance. As demonstrated in Figure 4d, Design 4 (580.98 mJ) significantly outperformed Design 3 (126.7 mJ) from the second cycle onwards, achieving an energy absorption enhancement

of over 358.5%. These results underscore the importance of geometric tuning in activating the CIS mechanism.

3.3. Mechanism elucidation via FEA

To elucidate the intrinsic mechanisms driving the differences in energy absorption caused by different deformation modes and to clarify the specific role of the TPU sheet, FEA was employed to investigate the metamaterial from the perspectives of material strain distribution and energy evolution. As illustrated in Figure 5a and b, Design 3 exhibits localised deformation mechanism (CIB). At an initial compression of $\delta = 1.4$ mm, strain is primarily concentrated at the loading interfaces and vertical hinges. As loading progresses ($\delta = 9.5$ mm), the inward rotation of rigid blocks intensifies the bending of TPU sheets, resulting in complete structural densification where sheets are compacted rather than stretched. Upon unloading, the lattice fails to recover, leaving visually buckled TPU sheets and residual strains in the hinges.

In distinct contrast, Design 4 exhibits typical CIS deformation characteristics (Figure 5c and d). At $\delta = 1.4$ mm, the rigid blocks undergo slight outward rotation, circumventing the bending of TPU sheets. As compression intensifies, this rotation drives the uniform stretching of the TPU sheets, yielding tensile strains of ~30%. At the maximum displacement ($\delta = 9.5$ mm), the sheets are maximally elongated with tensile strains increasing to approximately 40%. This 'activation' allows the material to fully utilise its viscoelastic damping capacity. Upon unloading, Design 4 demonstrates near-complete recovery.

Multi-cycle energy quantification (Figure 5e and f) further confirms this difference and validates the stabilisation trends. For Design 3, the peak Strain Energy (SE) stabilised at a low level (~171.5 mJ), and the Creep Dissipation Energy (CDE) of the first cycle was 196.24 mJ, with a small increment to 307.82 mJ after three cycles. Conversely, Design 4 exhibited significantly superior energy performance attributed to the extensive TPU sheet stretching. Its cumulative CDE reached 890.62 mJ after three cycles, with an average increase of 267.15% relative to Design 3. Furthermore, the peak SE was maintained at ~409.18 mJ (a 138.59% increase). This simulated evolution-characterised by rapid initial dissipation followed by steady accumulation – accurately captures the initial stress-softening behaviour and aligns well with the experimental energy absorption trends (Figure 4d). These substantial enhancements confirm that the CIS mechanism effectively maximises both the elastic storage and viscous dissipation capabilities compared to the CIB deformation mode.

3.4. Investigation of size effects in 2.5D CIS metamaterials

To ensure the scalability and robustness of the proposed CIS mechanism, it is essential to clarify how the structural response evolves with unit cell partitioning under a fixed macroscopic size. In practical energy-absorbing applications, the external dimensions of a component are often constrained, while internal architectural refinement offers a feasible pathway to tailor mechanical performance. Motivated by this consideration, the size effect of the proposed metamaterial is systematically investigated in Figure 6. Figure 6 examines the size effect by varying the number of unit cells while maintaining an identical overall geometry. To preserve the same external dimensions for all specimens, the unit cell size is correspondingly adjusted. Three configurations were fabricated and tested, namely 2×2, 3×3, and 4×4 lattices, with square unit cell edge lengths of 2.0, 1.3, and 1.0 cm, respectively. Importantly, TPU sheets are embedded within every unit cell across all configurations, ensuring that the compression-to-tension transformation mechanism is consistently activated throughout the entire structure.

Figure 6a illustrates the deformation sequence of the 2×2 metamaterial under quasi-static compression. Despite its relatively large unit cell size, the structure exhibits a deformation mode consistent with that observed in designs featuring smaller unit cells (Figure 5c). At the initial compression stage, the centrally located TPU sheets are subjected to compressive loading and undergo out-of-plane buckling. As the applied displacement increases and a critical state is reached, the buckled TPU sheets are subsequently stretched, triggering the compression-to-tension transition. This transition enables sustained energy dissipation through tensile deformation of the TPU sheets. The corresponding finite element simulation results are shown in Figure 6b, demonstrating good agreement with the experimental observations.

The deformation behaviour of the 3×3 metamaterial is presented in Figure 6c. Overall, its deformation mode closely resembles that of the 2×2 configuration. The structure initially experiences compressive deformation, followed by buckling of the TPU sheets. Upon reaching the critical deformation point, the TPU sheets transition into tension, contributing effectively to energy absorption. With continued compression, the rotating square units progressively close, eventually leading to a fully compacted state. The corresponding numerical simulation results are provided in Figure 6d, accurately capturing the experimentally observed deformation sequence.

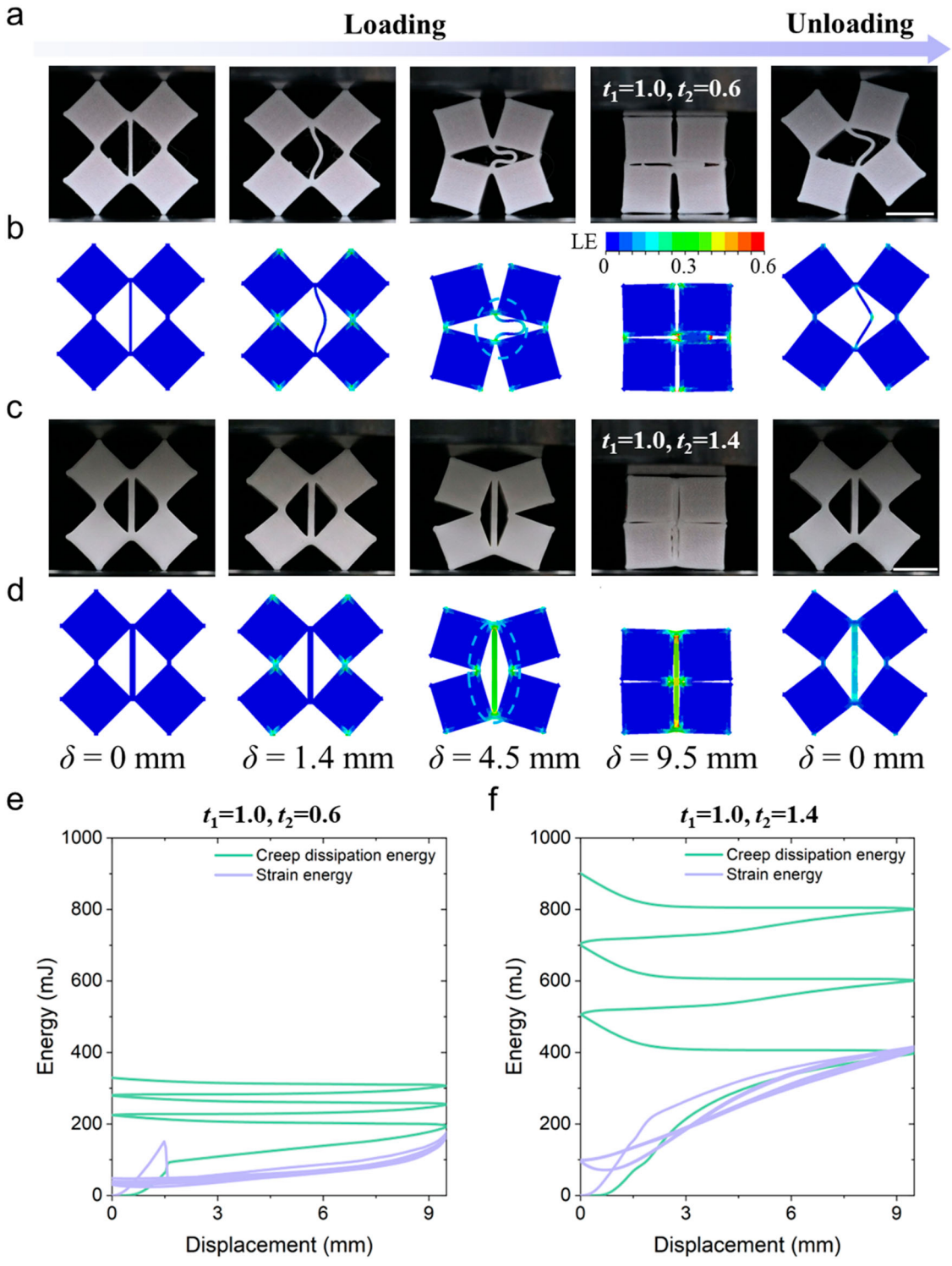

Figure 5. Finite element analysis of energy absorption mechanisms across different deformation modes. (**a**) Experimental loading-unloading sequence and (**b**) corresponding FE simulation contours for Design 3 (t_1 = 1.0 mm, t_2 = 0.6 mm). (**c**) Experimental loading-unloading sequence and (**d**) corresponding FE simulation contours for Design 4 (t_1 = 1.0 mm, t_2 = 1.4 mm). (**e**) Energy-displacement curves of Design 3 obtained from FEA over 3 loading-unloading cycles. (**f**) Energy-displacement curves of Design 4 obtained from FEA over 3 loading-unloading cycles. Scale bar: 10 mm.

In contrast, the 4 × 4 metamaterial, shown in Figure 6e, exhibits a more complex and progressive deformation mode. This behaviour is primarily attributed to the increased number of unit cells along the height direction, which induces a sequential collapse process during compression. Specifically, the upper portion of

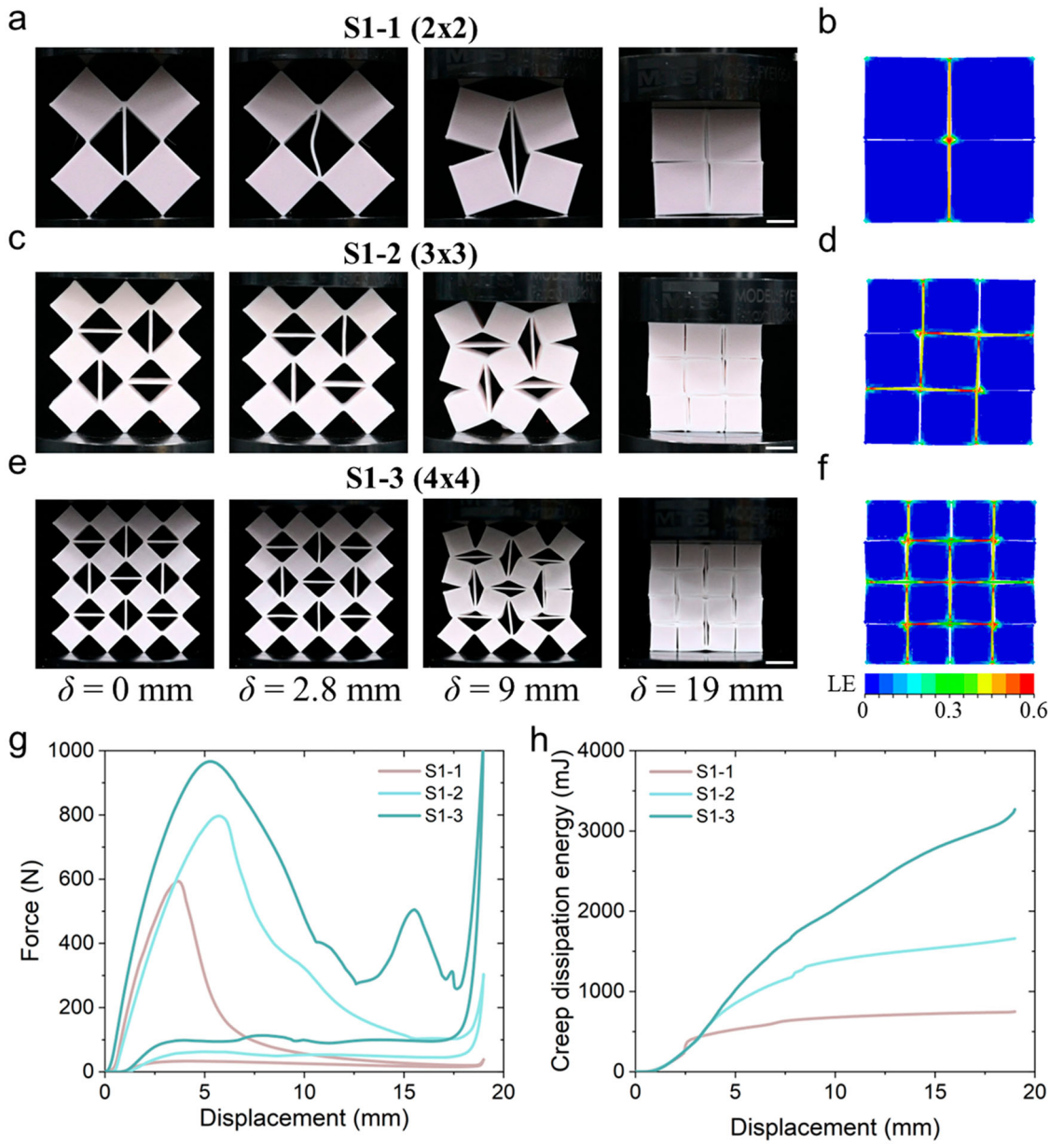

Figure 6. Size effects of the 2.5D CIS metamaterial under fixed macroscopic dimensions. (**a**) Experimental deformation sequence of the 2 × 2 lattice under quasi-static compression. (**b**) Corresponding FE simulation contour of the 2 × 2 lattice. (**c**) Experimental deformation process of the 3 × 3 lattice. (**d**) FE simulation contour of the 3 × 3 lattice. (**e**) Experimental deformation sequence of the 4 × 4 lattice. (**f**) Corresponding FE simulation contour of the 4 × 4 lattice. (**g**) The experimental force – displacement curves of the three lattices. (**h**) Evolution of displacement versus creep-dissipated energy extracted from FE simulations. Scale bar: 10 mm.

the structure closes first, followed by gradual closure of the lower portion, resulting in a layer-by-layer deformation pattern. Such progressive deformation effectively delays global instability and promotes more uniform energy dissipation throughout the structure. The corresponding finite element simulation results are shown in Figure 6f, confirming the consistency of this deformation behaviour.

Figure 6g compares the force-displacement responses of the three configurations. Under identical external dimensions, increasing the number of unit cells (i.e. decreasing the unit cell size) leads to a higher peak force, a delayed buckling strain, and a more complex deformation pathway. Both the 2 × 2 and 3 × 3 structures exhibit a single dominant peak force, whereas the 4 × 4 structure displays two distinct peak forces, corresponding to its staged deformation mode. Further parametric investigations, discussed later in Figure 8, reveal that increasing the number of unit cells along the height direction results in a corresponding increase in the number of peak forces in the force–displacement response. Moreover, for structures with

identical macroscopic dimensions, increasing the unit cell number significantly enhances the energy dissipation capacity, as reflected by the enlarged area enclosed by the force-displacement curves. Quantitatively, the 3×3 assembly absorbed 5184.68 mJ, representing approximately a 2.32-fold increase over the 2×2 structure, while the 4×4 assembly absorbed 8316.74 mJ, achieving a remarkable 3.72-fold increase compared to the 2×2 baseline. This performance enhancement stems not only from the increased cell count but also from the higher volumetric density of the functional TPU sheets capable of compression-to-tension conversion. As the unit cell size decreases, the total effective length of the TPU sheets increases, leading to greater energy dissipation via viscoelastic creep (Figure 6h). These factors synergistically endow CIS metamaterials with superior and more stable energy absorption performance.

3.5. Investigation of gradient design of TPU sheet in 2.5D CIS metamaterials

To further enhance the controllability of deformation and energy dissipation performance, the influence of material grading within the unit cells is investigated in Figure 7. While the macroscopic dimensions and overall lattice remain unchanged, introducing thickness gradients in the embedded TPU sheets provides an effective strategy to tailor the local stiffness distribution and, consequently, the global deformation sequence. Such a gradient design is particularly attractive for reusable energy-absorbing systems, where progressive collapse and stable force response are highly desirable.

Figure 7 compares three 4×4 metamaterial configurations with identical unit cell geometry and a square unit cell edge length of 1.0 cm. The three designs differ only in the arrangement and thickness distribution of the embedded TPU sheets. Specifically, Figure 7a shows the experimental deformation mode of a structure containing only vertically oriented TPU sheets, with all horizontal TPU sheets removed. The corresponding finite element simulation results are presented in Figure 7b. In this configuration, the absence of horizontal constraints leads to early global buckling, resulting in a relatively low peak force and limited energy dissipation.

Figure 7c and d present the experimental and numerical deformation sequences of the reference structure with both vertical and horizontal TPU sheets embedded in each unit cell. This configuration corresponds to the previously studied 4×4 lattice discussed in Figure 6e–f. The structure exhibits a progressive, layer-by-layer collapse initiated from the upper region, followed by gradual compaction of the lower layers. The deformation mode remains consistent between experiments and simulations, confirming the robustness of the CIS mechanism in this configuration.

In Figure 7e and f, a thickness-gradient design is formally introduced. The TPU sheet thickness is varied along the height direction, with the top layer set to 1 mm, the middle layer to 2 mm, and the bottom layer to 3 mm. The experimental deformation sequence in Figure 7e clearly demonstrates that the deformation order can be effectively programmed through this gradient design. Buckling and subsequent CIS activation first occur in the upper layer with thinner TPU sheets, followed sequentially by the middle and bottom layers as the applied displacement increases. This controlled, sequential collapse enables stable and efficient energy absorption through a progressive deformation process. The corresponding finite element simulation results in Figure 7f accurately reproduce the experimentally observed behaviour. Notably, this design strategy can be readily extended to structures with a larger number of layers (e.g. ten or more), allowing precise control of deformation progression from the topmost layer to the bottommost layer.

Figure 7g compares the force–displacement responses of the three configurations. The structure with only vertical TPU sheets (Figure 7a) exhibits the lowest peak force and the smallest energy dissipation capacity. Introducing both vertical and horizontal TPU sheets (Figure 7c) significantly increases the peak force, delays the onset of buckling, and enhances the absorbed energy. In this reference configuration, two peak forces are observed: the first peak is associated with global structural buckling, while the second peak arises from localised buckling of the bottom layer.

The gradient design shown in Figure 7e also exhibits two peak forces; however, its mechanical response is markedly different. The first peak force is comparable to that of the uniform-thickness structure in Figure 7c and is similarly governed by global buckling. In contrast, the second peak force is substantially higher, resulting from the buckling of the bottom layer with thicker TPU sheets, which require a much larger force to activate. Consequently, the area enclosed by the force–displacement curve is dramatically increased. At a displacement of approximately 15 mm, the peak force of the uniform structure (Figure 7c) is around 505.2 N, whereas the gradient structure (Figure 7e) reaches a peak force of approximately 1699.0 N. Overall, the total energy dissipation of the gradient design is nearly 1.77 times that of the uniform-thickness configuration.

Finally, Figure 7h presents the evolution of displacement versus creep-dissipated energy extracted from the numerical simulations. For the structures shown in

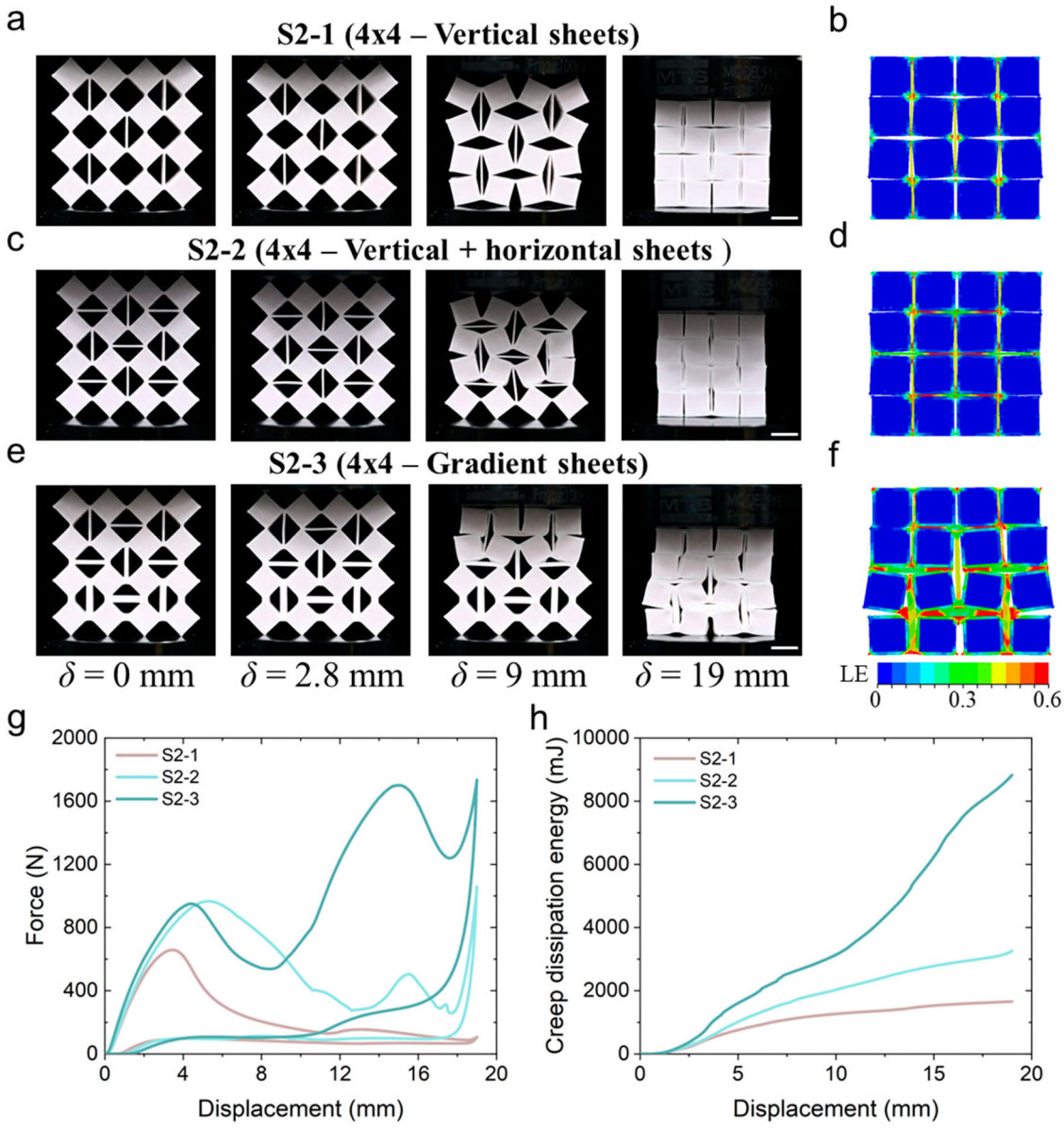

Figure 7. Effect of TPU sheet thickness grading on the deformation behaviour and energy absorption performance of the 2.5D CIS metamaterial. (a) Experimental deformation sequence of the structure containing only vertically oriented TPU sheets. (b) Corresponding FE simulation contour of the vertical-sheet-only configuration. (c) Experimental deformation sequence of the reference structure with both vertical and horizontal TPU sheets embedded in each unit cell. (d) Corresponding FE simulation contour of the uniform-thickness structure. (e) Experimental deformation sequence of the thickness-gradient structure, in which the TPU sheet thickness increases along the height direction (top: 1 mm, middle: 2 mm, bottom: 3 mm). (f) Corresponding FE simulation contour of the gradient design. (g) The experimental force – displacement curves of the three configurations. (h) Evolution of displacement versus creep-dissipated energy extracted from FE simulations. Scale bar: 10 mm.

Figure 7a and c, the growth rate of creep-dissipated energy gradually decreases with increasing displacement, indicating a saturation of energy dissipation capability. In contrast, the gradient structure in Figure 7e exhibits a pronounced increase in creep-dissipated energy during the final collapse of the bottom layer. This rapid energy dissipation highlights the effectiveness of the thickness-gradient strategy in achieving superior and sustained energy absorption performance.

3.6. Investigation of geometric aspect ratio in 2.5D CIS metamaterials

To further demonstrate the role of geometric aspect ratio on the deformation mode and energy dissipation performance of the proposed CIS metamaterials, the effect of structural height is systematically investigated in Figure 8. In practical energy-absorbing applications, increasing the number of unit cells along the loading

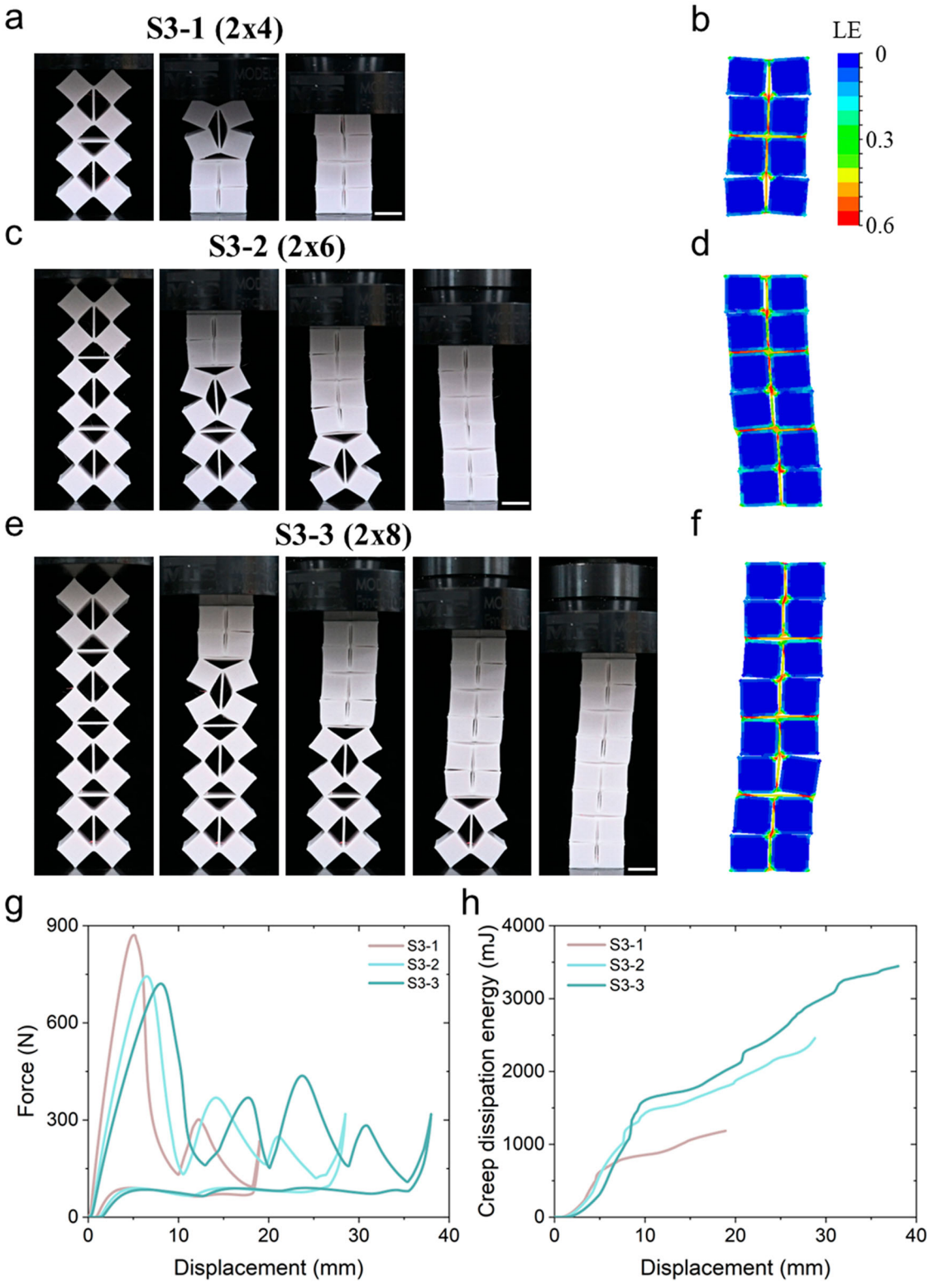

Figure 8. Effect of geometric aspect ratio on the deformation behaviour and energy absorption performance of the CIS metamaterial. (**a**) Experimental deformation sequence of the 2×4 lattice. (**b**) Corresponding FE simulation contour of the 2×4 lattice. (**c**) Experimental deformation sequence of the 2×6 lattice. (**d**) Corresponding FE simulation contour of the 2×6 lattice. (**e**) Experimental deformation sequence of the 2×8 lattice. (**f**) Corresponding FE simulation contour of the 2×8 lattice. (**g**) The experimental force – displacement curves of the three lattices. (**h**) Displacement versus creep-dissipated energy extracted from FE simulations. Scale bar: 10 mm.

direction provides an effective strategy to tailor the deformation sequence and force response.

Starting from the 2 × 2 lattice shown in Figure 5c, the thickness of the specimen is increased from 1 cm to 2 cm to suppress global out-of-plane buckling along the thickness direction, thereby ensuring stable uniaxial compression during testing. The original 2 × 2 unit-cell arrangement is then extended along the height direction to form 2 × 4, 2 × 6, and 2 × 8 lattices, while keeping the unit cell geometry unchanged. As a result, the number of unit cells along the loading direction increases from 2 to 4, 6, and 8, respectively.

Figures 8a and b present the experimental and numerical deformation sequences of the 2 × 4 metamaterial. Upon compression, deformation initiates from the bottom region, where the square units begin to rotate and progressively close. As the applied displacement increases, the deformation propagates upward in a sequential manner until the entire structure becomes compacted. The finite element (FE) simulation results in Figure 8b show excellent agreement with the experimental observations. The deformation behaviour of the 2 × 6 metamaterial is shown in Figure 8c and d. In this taller structure, the initiation of deformation is not deterministic and may occur from either the top or bottom layers, depending on slight geometric imperfections and loading conditions. In the representative case shown here, deformation initiates from the top layer: the uppermost square units rotate and close first, followed by successive activation of the underlying layers, leading to a progressive collapse along the height direction. The corresponding FE simulation results in Figure 8d accurately capture this deformation sequence. A similar deformation trend is observed for the 2 × 8 metamaterial, as shown in Figure 8e and f. The deformation again starts from the topmost layer and gradually propagates downward, resulting in a well-defined layer-by-layer collapse process. The numerical simulations in Figure 8f are in close agreement with the experimental results, confirming the robustness of the predicted deformation mechanism across different aspect ratios.

Figure 8g compares the force–displacement responses of the three lattices. As the number of unit cells along the height direction increases, the force–displacement curves exhibit an increasing number of distinct peak forces. Specifically, the 2 × 4 structure displays two peak forces, the 2 × 6 structure exhibits three peak forces, and the 2 × 8 structure shows four peak forces. This observation suggests that when the structure contains n unit cells along the loading direction, the number of force peaks scales approximately as n/2, reflecting the staged activation of successive deformation layers.

In addition, increasing the structural height leads to a systematic reduction in the initial stiffness and the magnitude of the first peak force. This trend is evidenced by the decreasing slope of the force–displacement curves and the progressively lower first peak force observed in Figure 8g as the height increases. Furthermore, both the buckling displacement and the maximum attainable displacement increase with structural height. The 2 × 4 structure reaches a maximum displacement of 19 mm, whereas the 2 × 6 and 2 × 8 structures can sustain displacements of approximately 28.5 and 38 mm, respectively, before full compaction. These trends are also reflected in the delayed onset of buckling for taller structures. Finally, Figure 8h illustrates the evolution of CDE as a function of displacement, as derived from the numerical simulations. In sharp contrast to the 2 × 4 configuration, the taller 2 × 6 and 2 × 8 configurations are capable of accommodating significantly larger compression strokes prior to reaching full densification. This extended deformability underscores their superior potential for total energy absorption, particularly in application scenarios necessitating substantial deformation ranges.

3.7. From 2.5D to cylindrical 3D CIS metamaterials

To further investigate the applicability of the proposed CIS metamaterial in three-dimensional load-bearing configurations, the energy dissipation behaviour of a fully three-dimensional structure is investigated in Figure 9. While the structures discussed before are quasi-2.5D lattices, practical energy-absorbing components often require closed, self-supporting 3D geometries to achieve enhanced load capacity, stability, and reusability. Motivated by this consideration, the 2.5D gradient structure shown in Figure 8e is extended into a cylindrical 3D metamaterial.

Figure 9a illustrates the fabrication process of the 3D CIS metamaterial. Specifically, six identical 2.5D structures (based on the 2 × 8 lattice in Figure 8e) are first arranged laterally and connected via designed linking features, forming a planar sheet during multimaterial 3D printing. After printing, the flat sheet is rolled into a closed cylindrical configuration and the two free edges are bonded together using adhesive, resulting in a self-supporting tubular metamaterial.

The quasi-static compression behaviour of the cylindrical 3D metamaterial is shown in Figure 9b. Upon loading, deformation initiates from the bottom layer of the cylinder, where the square units begin to rotate and progressively close. As the applied displacement increases, the deformation propagates upward in a layer-by-layer manner, closely resembling the

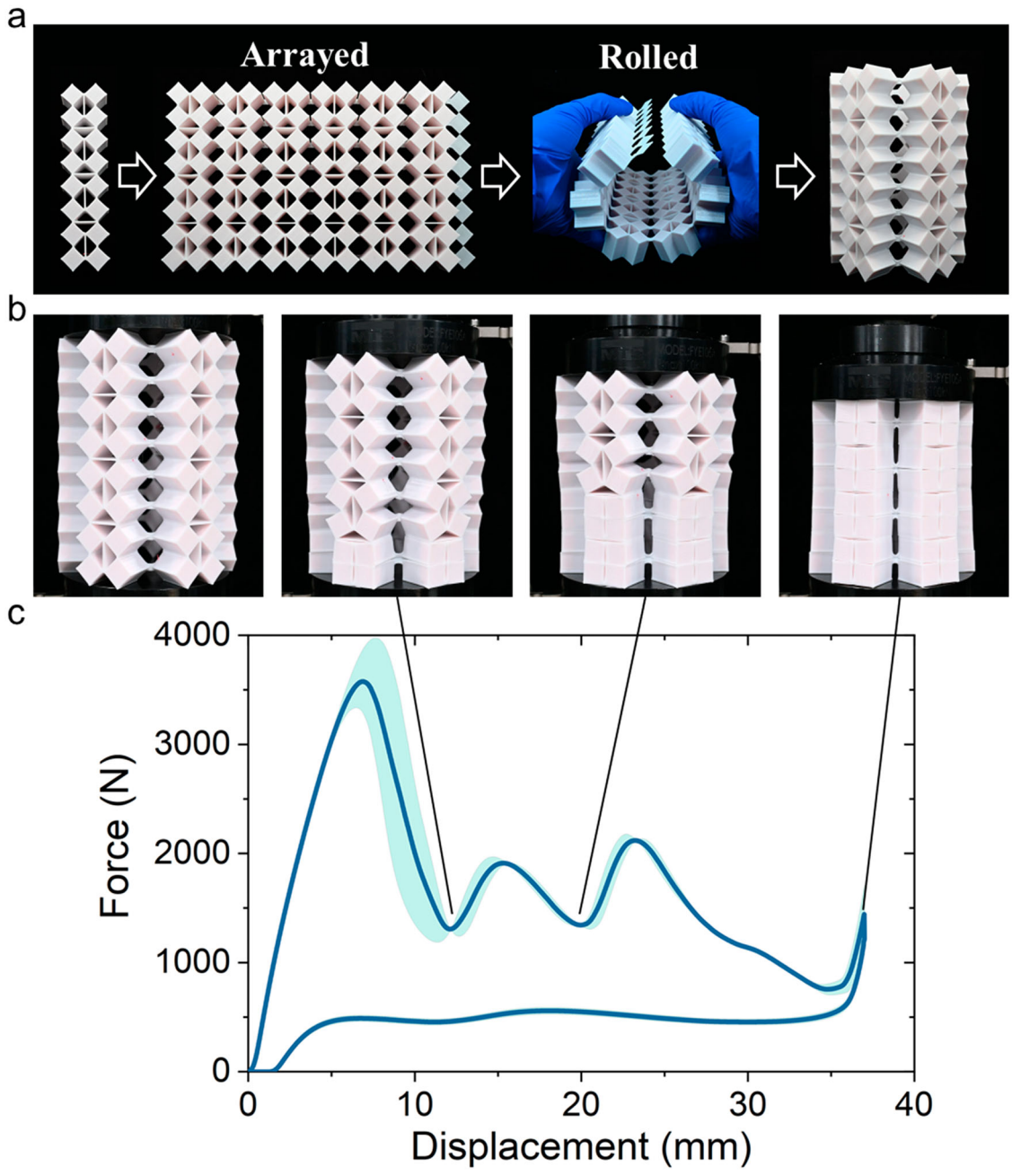

Figure 9. Three-dimensional cylindrical CIS metamaterial and its energy absorption performance. (**a**) Fabrication process of the 3D cylindrical metamaterial. (**b**) Experimental deformation sequence of the cylindrical metamaterial under quasi-static axial compression. (**c**) The average experimental force – displacement response of the 3D cylindrical metamaterial (shaded area represents confidence interval).

progressive collapse observed in the corresponding 2.5D gradient structure (Figure 8e). This sequential collapse continues until the topmost layer is activated and the entire cylindrical structure reaches a fully compacted state. Notably, the closed-ring topology effectively suppresses global instability and promotes a highly stable deformation mode under axial compression.

Figure 9c presents the force–displacement response of the 3D cylindrical metamaterial. The solid curve represents the mean force–displacement response obtained from three independent quasi-static compression tests, while the shaded region denotes the corresponding confidence interval, reflecting the experimental variability and repeatability of the mechanical response. Compared with the corresponding 2.5D structure, the 3D lattice metamaterial exhibits a substantially higher load-bearing capacity while retaining a progressive and stable force response. The first

peak force of the cylindrical structure is approximately six times that of the 2.5D gradient structure in Figure 8e, consistent with the sixfold circumferential replication of the unit lattice. In addition to the significantly increased peak force, the force–displacement curve encloses a much larger area, reaching 45,049.5 mJ, which indicates a greatly enhanced energy absorption capacity. Importantly, after unloading, the structure exhibits excellent recoverability with minimal residual deformation, highlighting its strong potential for reusable energy absorption applications.

4. Conclusions

In summary, this study proposed a multi-material 3D printed reusable, high-performance energy-absorbing metamaterial based on a CIS mechanism. By leveraging multi-material additive manufacturing with a robust 'wrapping' encapsulation strategy, we successfully integrated rigid kinematic skeletons with soft viscoelastic dissipation sheets, effectively overcoming common limitations in traditional structures such as one-time use, inherent instability, and weak interfaces. We demonstrated the interplay between hinge resistance and tensioning forces, establishing a critical geometric design map that distinguishes the efficient CIS mode from the CIB mode. This geometric regulation ensures that global compressive loads are reliably converted into the uniform stretching of the embedded viscoelastic polymer network, thereby maximising energy absorption.

The optimised CIS metamaterial exhibited exceptional mechanical performance and durability. Compared to the CIB mode, the proposed CIS mode achieved an energy absorption enhancement exceeding 358.5% and maintained structural integrity with stable hysteresis loops over 500 mechanical loading cycles. Furthermore, we demonstrated that the mechanical response of this system is highly tunable. By introducing intra-cell material gradients and manipulating structural aspect ratios, the deformation sequence can be deterministically programmed – such as achieving layer-wise progressive densification – to customise force-displacement signatures for specific loading scenarios. The successful extension from 2.5D unit cells to a macroscopic 3D cylindrical lattice metamaterial further validated the scalability of the concept, exhibiting significantly enhanced load-bearing capacity and total energy absorption suitable for practical engineering applications.

Despite the robust framework established here for CIS metamaterials, several avenues for future investigation remain. First, to mitigate the current sensitivity of deformation modes to boundary conditions, optimisation strategies will be developed to ensure performance consistency across various interfaces. Building on this kinematic stability, the programmability of the system can be further expanded by refining the deterministic control of rotation pathways. Adopting complex hinge architectures, such as the self-guided pathways proposed by Coulais et al. [53], or incorporating nonlinear hinge geometries into the CIS framework could enable multi-step, sequential deformation modes, thereby unlocking new potentials for energy-absorbing metamaterials. Finally, a critical consideration involves the thermal effects of viscoelastic damping in high-frequency scenarios; since substantial energy is dissipated as internal heat within the TPU matrix, rapid cycling can lead to thermal softening, decreasing stiffness and recovery force. Thus, for applications beyond discrete impacts – particularly those requiring high-frequency damping – thermal management will be essential to maintain a stable mechanical response.

Acknowledgements

Xu Song acknowledges the financial support of the Hong Kong Research Grants Council (No. C4074-22G), the Hong Kong Special Administrative Region University Grants Committee - General Research Fund (CUHK14209523 and CUHK14206925), and the Innovation and Technology Commission - Innovation and Technology Support Programme (ITSP) ITP/058/23TP. Wei-Hsin Liao acknowledges the financial support of the Hong Kong Research Grants Council (Nos. C4074-22G and STG5/E-103/24-R) and The Chinese University of Hong Kong (Project No. 3110174).

Author contributions

CRediT: **Haitao Ye:** Conceptualization, Data curation, Formal analysis, Investigation, Methodology, Software, Validation, Writing – original draft, Writing – review & editing; **Xingjian Huang:** Conceptualization, Formal analysis, Investigation, Methodology, Software, Validation; **Liuchao Jin:** Conceptualization, Methodology, Writing – original draft; **Sicong Zhou:** Investigation, Resources; **Guoquan Xie:** Investigation, Resources; **Zongxin Hu:** Investigation, Resources, Software; **Rui Li:** Conceptualization, Resources, Software; **Haoming Mo:** Investigation, Methodology, Resources; **Shitong Fang:** Conceptualization, Resources; **Wei-Hsin Liao:** Conceptualization, Resources, Writing – review & editing; **Qi Ge:** Conceptualization, Resources, Writing – review & editing; **Xu Song:** Conceptualization, Funding acquisition, Methodology, Supervision, Writing – original draft, Writing – review & editing.

Disclosure statement

No potential conflict of interest was reported by the author(s).

Funding

This work was supported by Hong Kong Special Administrative Region University Grants Committee - General Research Fund: [Grant Number CUHK14209523 and CUHK14206925]; Hong Kong Research Grants Council: [Grant Number C4074-22G]; Hong Kong Research Grants Council: [Grant Number C4074-22G and STG5/E-103/24-R]; The Chinese University of Hong Kong: [Grant Number 3110174]; Innovation and Technology Commission - Innovation and Technology Support Programme: [Grant Number ITP/058/23TP].

Data availability statement

The data that support the findings of this study are openly available in Figshare at: https://doi.org/10.6084/m9.figshare.31267861.

References

[1] Lu G, Yu T. *Energy absorption of structures and materials*. Abington: Woodhead Publishing Limited; 2003.
[2] Gao Q, Ni X, Liu R, et al. Auxetic structures for energy absorption: A review on design, manufacturing, optimization, and applications. J Intell Mater Syst Struct. 2026. doi:10.1177/1045389X251381598
[3] Frenzel T, Findeisen C, Kadic M, et al. Tailored buckling microlattices as reusable light-weight shock absorbers. Adv Mater. 2016;28(28):5865–5870. doi:10.1002/adma.201600610
[4] Ramirez B, Kingstedt O, Crum R, et al. Tailoring the rate-sensitivity of low density polyurea foams through cell wall aperture size. J Appl Phys. 2017;121(22):225107. doi:10.1063/1.4985280
[5] Cui L, Kiernan S, Gilchrist MD. Designing the energy absorption capacity of functionally graded foam materials. Mater Sci Eng A. 2009;507(1-2):215–225. doi:10.1016/j.msea.2008.12.011
[6] Wu S, Wang R, Jin L, et al. Digital light processing 3D printing of large-scale and crack-free ceramics with perforated internal honeycomb structures. Virtual Phys Prototyp. 2025;20(1):e2589472. doi:10.1080/17452759.2025.2589472
[7] Wang R, Ye H, Cheng J, et al. Ultrastrong and damage-tolerant ceramic architectures via 3D printing. Addit Manuf. 2023;61:103361. doi:10.1016/j.addma.2022.103361
[8] Liu W, Janbaz S, Dykstra D, et al. Harnessing plasticity in sequential metamaterials for ideal shock absorption. Nature. 2024;634(8035):842–847. doi:10.1038/s41586-024-08037-0
[9] Ma WWS, Zhang L, Ding J, et al. Rib-reinforced ultralight and ultra-strong shell lattices. Adv Sci. 2026:e18357. doi:10.1002/advs.202518357
[10] Ding J, Ma Q, Li X, et al. Imperfection-enabled strengthening of ultra-lightweight lattice materials. Adv Sci. 2024;11(41):2402727. doi:10.1002/advs.202402727
[11] Chen Y, Jin L. Reusable energy-absorbing architected materials harnessing snapping-back buckling of wide hyperelastic columns. Adv Funct Mater. 2021;31(31):2102113. doi:10.1002/adfm.202102113
[12] Fu K, Zhao Z, Jin L. Programmable granular metamaterials for reusable energy absorption. Adv Funct Mater. 2019;29(32):1901258. doi:10.1002/adfm.201901258
[13] Meza LR, Das S, Greer JR. Strong, lightweight, and recoverable three-dimensional ceramic nanolattices. Science. 2014;345(6202):1322–1326. doi:10.1126/science.1255908
[14] Schaedler TA, Jacobsen AJ, Torrents A, et al. Ultralight metallic microlattices. Science. 2011;334(6058):962–965. doi:10.1126/science.1211649
[15] Salari-Sharif L, Schaedler TA, Valdevit L. Energy dissipation mechanisms in hollow metallic microlattices. J Mater Res. 2014;29(16):1755–1770. doi:10.1557/jmr.2014.226
[16] Zhou T, Huang C, Miao Z, et al. Intrinsically multi-stable spatial linkages. Adv Sci. 2024;11(41):2402127. doi:10.1002/advs.202402127
[17] Fang H, Chu SCA, Xia Y, et al. Programmable self-locking origami mechanical metamaterials. Adv Mater. 2018;30(15):1706311. doi:10.1002/adma.201706311
[18] Shan S, Kang SH, Raney JR, et al. Multistable architected materials for trapping elastic strain energy. Adv Mater. 2015;27(29):4296–4301. doi:10.1002/adma.201501708
[19] Yasuda H, Yang J. Reentrant origami-based metamaterials with negative poisson's ratio and bistability. Phys Rev Lett. 2015;114(18):185502. doi:10.1103/PhysRevLett.114.185502
[20] Hu Z, Ding J, Ding S, et al. Machine learning – enabled inverse design of shell-based lattice metamaterials with optimal sound and energy absorption. Virtual Phys Prototyp. 2024;19(1):e2412198. doi:10.1080/17452759.2024.2412198
[21] Wang Y, Sha W, Xiao M, et al. Thermal metamaterials with configurable mechanical properties. Adv Sci. 2024;11(40):2406116. doi:10.1002/advs.202406116
[22] Xu J, Xiao M, Gao L. Inverse design of structures with accurately programmable nonlinear mechanical responses by topology optimization. Comput Methods Appl Mech Eng. 2025;446:118243. doi:10.1016/j.cma.2025.118243
[23] Jiao P, Mueller J, Raney JR, et al. Mechanical metamaterials and beyond. Nat Commun. 2023;14(1):6004. doi:10.1038/s41467-023-41679-8
[24] Bertoldi K, Vitelli V, Christensen J, et al. Flexible mechanical metamaterials. Nat Rev Mater. 2017;2(11):1–11. doi:10.1038/natrevmats.2017.66
[25] Jin L, Yu S, Cheng J, et al. Machine learning powered inverse design for strain fields of hierarchical architectures. Compos B Eng. 2025;299:112372. doi:10.1016/j.compositesb.2025.112372
[26] Meng Z, Chen W, Mei T, et al. Bistability-based foldable origami mechanical logic gates. Extreme Mech Lett. 2021;43:101180. doi:10.1016/j.eml.2021.101180
[27] Li Z, Zeng K, Guo Z, et al. All-in-one: An interwoven dual-phase strategy for acousto-mechanical multifunctionality in microlattice metamaterials. Adv Funct Mater. 2025;35(20):2420207. doi:10.1002/adfm.202420207
[28] Qiu J, Lang JH, Slocum AH. A curved-beam bistable mechanism. J Microelectromech Syst. 2004;13(2):137–146. doi:10.1109/JMEMS.2004.825308
[29] Yang H, Zhang J, Wang J, et al. Delocalized deformation enhanced reusable energy absorption metamaterials

based on bistable tensegrity. Adv Funct Mater. 2025; 35(5):2410217. doi:10.1002/adfm.202410217
[30] Li J, Chen Z, Li Q, et al. Harnessing friction in intertwined structures for high-capacity reusable energy-absorbing architected materials. Adv Sci. 2022;9(13):2105769. doi:10.1002/advs.202105769
[31] Yuan S, Chua CK, Zhou K. 3D-printed mechanical metamaterials with high energy absorption. Adv Mater Technol. 2019;4(3):1800419. doi:10.1002/admt.201800419
[32] Zeng C, Liu L, Hu Y, et al. Stair-stepping mechanical metamaterials with programmable load plateaus. Adv Funct Mater. 2024;34(49):2408887. doi:10.1002/adfm.202408887
[33] Ahn D-G. Applications of laser assisted metal rapid tooling process to manufacture of molding & forming tools — state of the art. Int J Prec Eng Manuf. 2011; 12(5):925–938. doi:10.1007/s12541-011-0125-5
[34] Cheng J, Yu S, Wang R, et al. Digital light processing based multimaterial 3D printing: challenges, solutions and perspectives. Int J Extreme Manuf. 2024;6(4): 042006. doi:10.1088/2631-7990/ad4a2c
[35] Wang F, Bu H, Luo J, et al. Influence of different micropattern types on interface characteristic and mechanical property of CFRTP/aluminum alloy laser bonding joint. Int J Adv Manuf Technol. 2022;120(5-6):3543–3557. doi:10.1007/s00170-022-08748-6
[36] Xu W, Zhang M, Xu H, et al. INPR-Connector: interlocking negative poisson's ratio connectors design for deployable energy absorption structures. Compos B Eng. 2025; 297:112243. doi:10.1016/j.compositesb.2025.112243
[37] Liu Q, Ye H, Cheng J, et al. Stiffness-tunable origami structures via multimaterial three-dimensional printing. Acta Mech Solida Sin. 2023;36(4):582–593. doi:10.1007/s10338-023-00403-1
[38] Ye H, Liu Q, Cheng J, et al. Multimaterial 3D printed self-locking thick-panel origami metamaterials. Nat Commun. 2023;14(1):1607. doi:10.1038/s41467-023-37343-w
[39] Renaud C, Cros J-M, Feng Z-Q, et al. The yeoh model applied to the modeling of large deformation contact/impact problems. Int J Impact Eng. 2009;36(5):659–666. doi:10.1016/j.ijimpeng.2008.09.008
[40] Diani J, Fayolle B, Gilormini P. A review on the mullins effect. Eur Polym J. 2009;45(5):601–612. doi:10.1016/j.eurpolymj.2008.11.017
[41] Zheng X, Smith W, Jackson J, et al. Multiscale metallic metamaterials. Nat Mater. 2016;15(10):1100–1106. doi:10.1038/nmat4694
[42] Garland AP, Adstedt KM, Casias ZJ, et al. Coulombic friction in metamaterials to dissipate mechanical energy. Extreme Mech Lett. 2020;40:100847. doi:10.1016/j.eml.2020.100847
[43] Wang Y, Ramirez B, Carpenter K, et al. Architected lattices with adaptive energy absorption. Extreme Mech Lett. 2019;33:100557. doi:10.1016/j.eml.2019.100557
[44] Zhu S, Tan X, Wang B, et al. Bio-inspired multistable metamaterials with reusable large deformation and ultra-high mechanical performance. Extreme Mech Lett. 2019;32: 100548. doi:10.1016/j.eml.2019.100548
[45] Haghpanah B, Salari-Sharif L, Pourrajab P, et al. Multistable shape-reconfigurable architected materials. Adv Mater. 2016;28(36):7915–7920. doi:10.1002/adma.201601650
[46] Cheng Y, Li J, Qian X, et al. 3D printed recoverable honeycomb composites reinforced by continuous carbon fibers. Compos Struct. 2021;268:113974. doi:10.1016/j.compstruct.2021.113974
[47] Cooper CB, Joshipura ID, Parekh DP, et al. Toughening stretchable fibers via serial fracturing of a metallic core. Sci Adv. 2019;5(2):eaat4600. doi:10.1126/sciadv.aat4600
[48] Ling C, Cernicchi A, Gilchrist MD, et al. Mechanical behaviour of additively-manufactured polymeric octet-truss lattice structures under quasi-static and dynamic compressive loading. Mater Des. 2019;162:106–118. doi:10.1016/j.matdes.2018.11.035
[49] Aldoshan A, Khanna S. Effect of relative density on the dynamic compressive behavior of carbon nanotube reinforced aluminum foam. Mater Sci Eng A. 2017; 689:17–24. doi:10.1016/j.msea.2017.01.100
[50] Stanev L, Drenchev B, Yotov A, et al. Compressive properties and energy absorption behaviour of AlSi10Mg open-cell foam. J Mater Sci Technol. 2014;22:44–53.
[51] Li Z, Wang X, Zeng K, et al. Unprecedented mechanical wave energy absorption observed in multifunctional bioinspired architected metamaterials. NPG Asia Mater. 2024;16(1):45. doi:10.1038/s41427-024-00565-5
[52] Ding J, Wen Y, Wang Q, et al. Material-gradient enabled enhancement of strength and strain-hardening of lattice structures. Adv Sci. 2025;12(48):e11185. doi:10.1002/advs.202511185
[53] Coulais C, Sabbadini A, Vink F, et al. Multi-step self-guided pathways for shape-changing metamaterials. Nature. 2018;561(7724):512–515. doi:10.1038/s41586-018-0541-0